Wideband QAM-over-SMF/turbulent FSO downlinks in a PON architecture for ubiquitous connectivity

Dong-Nhat Nguyen[1], Luis Vallejo[2], Jan Bohata[1], Beatriz Ortega[2], Zabih Ghassemlooy[3] and Stanislav Zvanovec[1]

[1]Department of Electromagnetic Field, Czech Technical University in Prague, Technicka 2, 166 27, Prague, Czech Republic
[2]Instituto de Telecomunicaciones y Aplicaciones Multimedia, ITEAM, Universitat Politecnica de Valencia, Valencia 46022, Spain
[3]Optical Communication Research Group, Faculty of Engineering and Environment, Northumbria University, Newcastle upon Tyne NE1 8ST, United Kingdom

Corresponding author: Dong-Nhat Nguyen (e-mail: dongnhat@fel.cvut.cz).

Abstract

We propose and investigate for the first time a seamless millimeter-wave (mmW) radio-over-fiber (RoF) and radio-over-free-space optics (FSO)-based downlink for use in a passive optical network architecture using 4-, 16- and 64-quadrature amplitude modulation (QAM) for broadband wireless access (BWA) networks. The proposed system is implemented in both experiment and simulation to realize continuous and ubiquitous coverage in urban and rural areas. We outline, a proof-of-concept demonstration of 4-, 16- and 64-QAMs at data rates of 34, 67 and 100 Mb/s, respectively transmitted over a 15 km standard single-mode fiber (SMF), which is then optically up-converted to 25 GHz for transmission over a 10 km of SMF and a 2 m of FSO channel under a non-uniform turbulent condition. We show the measured error vector magnitude (EVM) values of 13, 9.2 and 7.3% for 4-, 16- and 64-QAM, respectively, which are below the corresponding standard EVM requirements and therefore confirm the practicality of the proposed hybrid system. Depending on the data rates, each modulation can be adaptively configured. We report a simulation of a 10 Gb/s 4- and 64-QAM hybrid RoF-FSO downlink under an extended non-uniform turbulence regime to verify the feasibility of the proposed scheme for use in practical applications. By implementing the decision-directed carrier phase recovery and linear electrical equalization, EVMs can be efficiently reduced below the required limits. We further evaluate the proposed system performance in terms of the bit error rates, constellation diagrams, received optical and mmW powers. Using state-of-the-art K-band power amplifiers and conical horn antennas, the maximum wireless transmission distance is estimated to be about 135 m for use in the last-mile BWA networks.

Keywords: Free-space optical communication, Fiber-FSO integrated system, atmospheric turbulence, millimeter-wave

1. INTRODUCTION

The widespread deployment of broadband wireless access (BWA) networks would not have been possible without the exploitation of optical fiber (OF) infrastructure. OF-based fronthaul links between the central stations (CS) and base stations (BS), which is also known as the radio-over-fiber (RoF) technology using the millimeter-wave (mmW) [1] and even terahertz-wave bands [2], are considered the most promising solution to provide higher capacity, lower latency, higher security and mobility in BWA networks. There are a number of techniques for optically generating a mmW signal including optical modulator-based up-conversion (MUC) [3] and optical heterodyning (OH) [4], which are the most well-known and widely reported in the literature. However, in RoF systems transmission of an optical mmW signal between CS and BS is less feasible, particularly in rural and remote areas (i.e., geographical constraints) due to the high deployment cost and damaged cables (road works or earthquakes, e.g., Great East Japan Earthquake in 2011). The free-space optical (FSO) communications technology [5] can be therefore adopted to solve the aforementioned issues in order to maintain seamless connectivity. FSO is also a potential solution for the last-mile access networks and an attractive substitute for both OF and radio frequency (RF) communication systems since it offers unique features such

as large bandwidth, license-free spectrum, high data rate R_b, easy and quick deployment. At present, compact FSO transceivers with an aperture diameter of 5 cm operating at a wavelength of 1550 nm, which is compatible with the C-band transmission window in OF communications, and R_b of up to 30 Gb/s over a FSO link length L of 1.5 km are commercially available [6]. The radio-over-FSO (RoFSO) technology was first introduced and demonstrated in 2006 as a possible option for OF links to transport RF signals over short distances in [7], where modulated analog RF signals in the frequency range of 46 to 870 MHz was transmitted over a 3 m indoor FSO link and characterized the key performance parameters (i.e., carrier-to-noise ratio and spurious free dynamic range). However, the effect of atmospheric turbulence (AT) was not considered. It is well-known that, the FSO link performance is highly affected by the AT strength, which is usually characterized by the refractive index structure parameter C_n^2 ($\mathrm{m}^{-2/3}$). In 2009, P. T. Dat *et al.*, carried out complete and long-term RoFSO measurements with RF in the frequency range of 450 kHz to 420 MHz over a link span of 1 km in an outdoor environment with AT and compared with the analytical model [8]. Both experimental and numerical results showed a good agreement even under a strong AT regime.

Seamless integration of RoF and RoFSO, abbreviated as RoF-FSO operating in the mmW band, have therefore become attractive for use in rural areas [9]–[11]. However, in these works the AT effect was not investigated. We recently also proposed and successfully demonstrated the RoF-FSO link over a wide frequency range (i.e., 25 – 40 GHz) for use in fifth-generation and beyond wireless networks in [12], [13], where both optical data modulation and mmW signal generation were concurrently held at CS. We carried out full system characterization under different AT conditions along the FSO link and showed that, the highest impact on the link performance is under AT evenly distributed along the propagation path, which resulted in an optical power penalty of 5 dB compared with the link with no AT.

Since the passive optical network (PON) technology is widely adopted by many operators worldwide due to a number of benefits, including energy-saving, scalability and signal security. It is therefore reasonable to integrate optical fronthaul links within PON architectures [14] in order to simultaneously provide multiple services via wireline and wireless links. The proposed system for use in the PON architecture to deliver different services simultaneously is shown in Fig. 1. In this regard, optical data modulation and mmW signal generation are implemented independently at the optical line terminal (OLT) and CS, respectively. In addition, this will further scale the system mobility and reduce the implementation cost for ubiquitous coverage to remote areas. The seamless system thus can be used to deliver the downstream basedband signal from OLT to the optical network unit (ONU) via a standard single-mode fiber (SMF1) and an optical splitter (OSP) for wireline services. For wireless services, the optical mmW generation using MUC is first generated at the CS and then distributed via another OSP to different areas e.g., urban and rural using SMF2 and hybrid SMF2-FSO, respectively. Note that, a range of modulation formats such as on-off-keying (OOK) and multilevel quadrature amplitude modulation (*M*-QAM) have been appraised as promising candidates for the downlink in future PONs [15]. Research works on optical fronthaul links in PON architectures at the system level are scarce. Very recently, C.-H. Yeh *et al.*, successfully demonstrated an integrated transmission for triple-play services of OF baseband, FSO baseband and 36 GHz mmW RoF using OOK signal at R_b of 10 Gb/s via the current PON architecture [16]. The obtained bit error rates (BERs) for all three transmissions were well below the forward-error correction (FEC) limit of 3.8×10^{-3}. As for the RoF downlink in [16], the OOK baseband signal was first modulated using a Mach-Zehnder modulator (MZM) and transmitted over a 25 km SMF, see SMF1 in Fig. 1, via the OLT. Note that, MZM offers improved overall system performance and therefore it has been employed in recent PON demonstrations [17]. To provide BWA in rural areas, the optically up-converted signal using MUC at the CS was transmitted over SMF2 (8 km) to the remote BS (RBS) i.e., remote radio head.

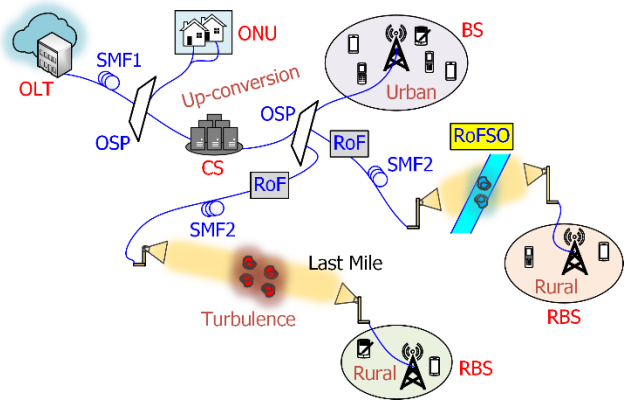

FIGURE 1. The proposed hybrid mmW RoF-FSO system in a PON architecture for providing ubiquitous coverage to urban and rural areas. OLT: optical line terminal, ONU: optical network unit, SMF: single-mode fiber, FSO: free-space optics, OSP: optical splitter, CS: central station, BS: base station and RBS: remote base station.

TABLE 1. RECENT ROF DOWNLINK DEMONSTRATIONS IN A PON ARCHITECTURE

mmW generation technique (band (GHz))	Modulation format	SMF1 length (km)	SMF2 length (km)	Year
OH (85)	OOK	10	5	2017 [18]
OH (76)	OOK	25	0	2019 [19]
MUC (36)	OOK	25	8	2019 [16]
MUC (25)	*M*-QAM	15	10	**This work**

Previous works on RoF links in PON using the OH technique have also been reported, which are summarized in Table 1. However, OOK is not spectrally efficient since it has

the required bandwidth equal to R_b. The next-generation BWA systems will generally use higher-order modulation formats to increase the spectral efficiency and therefore, achieve higher R_b. Without considering SMF2 in the network, the transmission link can be expected to deliver BWA to urban areas. It is worth to mention that, no RoFSO links have been examined in these works for the last-mile access networks. However, employing RoFSO in this architecture offer the followings:

i. High flexibility in network planning – due to the optical mmW signal generation and transmission being closer to the RF wireless segment.
ii. Improved power budget – lower loss of optical signal compared with the mmW signal, thus increased data rates or improved signal to noise ratio (SNR).

Inspired by the aforementioned technologies and to further contribute and advance this research topic, we explore for the first time the possibility of realizing a seamless integrated 25 GHz RoF-FSO downlink with square-shaped *M*-QAM (i.e., M = 4, 16 and 64) within a PON architecture for continuous and ubiquitous coverage in urban and rural areas. Note that the proposed link is compatible with the C-band in OF communications. To verify the feasibility of the hybrid system, we have carried out experimental works supported by numerical simulation.

We have also experimentally investigated the effect of non-uniform turbulence in an indoor environment using an AT chamber in which the link may experience in real practical outdoor environments. We then extend the proposed system with 4- and 64-QAM in terms of both L and R_b for use in urban and rural areas. However, at a high R_b, signals are more susceptible to channel impairments i.e., accumulated OF chromatic dispersion (CD) effect (i.e., in the SMF1 and SMF2). Therefore, to maintain high-quality mmW signals, we use conventional decision-directed carrier phase recovery and electrical equalization (CPR & EEQ) schemes at the receiver (Rx) to separately compensate for the CD effect and improve the transmission performance. Finally, we estimate the maximum reach of the mmW signal with commercially available components i.e., power amplifier (PA) and antennas (ANTs) in the RF K-band.

Therefore, the novel contributions of this paper are briefly summarized as follows:

- Proposing the RoF-FSO downlink in a PON architecture for use in urban and rural areas.
- Considering the effect of non-uniform AT in the FSO channel.
- Applying CPR and EEQ to compensate for the accumulated CD-induced ISI.
- Estimating the achievable mmW transmission distance for the indoor and last-mile applications in rural areas.

The remainder of the paper is organized as follows: Section 2 introduces the system model and basic concepts of the proposed hybrid systems. Section 3 presents the proof-of-concept experimental setup and results in rural areas, while Section 4 discusses the numerical simulation analysis for an extension of the proposed transmission link in both urban and rural areas. Finally, Section 5 concludes the study.

2. SYSTEM DESIGN AND THEORETICAL BACKGROUND

Fig. 2 illustrates the schematic diagram of the *M*-QAM hybrid mmW RoF-FSO downlink. As can be seen in Fig. 2, the optically modulated *M*-QAM signal is given by:

$$E_c(t) = A(t)exp(j\omega_c t) \quad (1)$$

where $A(t)$ represents the *M*-QAM data signal and $\omega_c = 2\pi f_c$ is the angular optical carrier frequency.

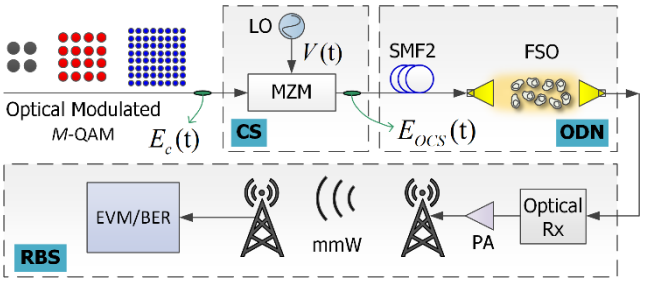

FIGURE 2. The simplified system model of a hybrid mmW RoF-FSO downlink for ubiquitous coverage to rural areas. LO: local oscillator, MZM: Mach-Zehnder modulator and PA: power amplifier.

Note that, for a given R_b, single-subcarrier square-shaped *M*-QAM bandwidth is $2/\log_2 M$ of the OOK bandwidth B_{OOK} [20]. Considering the same transmission condition, *M*-QAM suffers the optical power penalty relative to OOK expressed in dB is given as [20]:

$$P_p = 10log_{10}\left(\frac{2(\sqrt{M}-1)}{\sqrt{log_2 M}}\right) \quad (2)$$

For the same BER, 1.5 dB of additional optical power is required for 4-QAM compared with OOK. For 16- and 64-QAM (i.e., 1/2 and 1/3 of B_{OOK}, respectively), 4.8 and 7.6 dB of more optical power is required, respectively, thus having an impact on the link's power budget. However, using an avalanche photodiode (PD) at the Rx in both links of OF and FSO, there is a gain improvement of up to 7 dB compared with the PIN PD [5], [17]. Moreover, in practical next-generation optical fronthaul links, erbium-doped fiber amplifiers (EDFAs) may be used to share the same optical infrastructure with the current PON [17].

The *M*-QAM signals are then optically up-converted using a single-drive MZM and a RF local oscillator (LO) of $V(t) = V_{\mathrm{LO}}\cos\omega_{\mathrm{LO}}t$. Here, ω_{LO} and V_{LO} are the angular frequency

and amplitude of the LO. By controlling the bias voltage of the MZM and ω_{LO}, different modulated optical RF signals (i.e., with double-sideband, single-sideband and optical carrier suppression (OCS)) can be generated. In this work, the focus is on OCS since it has been shown to be the most robust against channel effects [21]. Details of derivations of realizing each configuration can be found in [22]. The externally modulated optical signal is expressed as [22]:

$$E_{OCS}(t) = \frac{\gamma}{2}A(t)\left\{J_1(m_h)\,exp\,j\left[(\omega_c + \omega_{LO})t + \frac{\pi}{2}\right] + J_1(m_h)\,exp\,j\left[(\omega_c - \omega_{LO})t + \frac{\pi}{2}\right]\right\} \quad (3)$$

where γ is the MZM insertion loss, J_1 is the first-order Bessel function and $m_h = \pi V_{LO}/V_\pi$ is the modulation index with V_π being the MZM switching voltage. By fine-tuning m_h, the optimal carrier suppression ratio (CSR), which is defined as the power ratio of optical power in the central carrier to that of the first sideband, can be adjusted. Low CSR implies a higher level optical carrier signal, which leads to the degradation of Rx sensitivity due to the dc components at the center wavelength [22]. $E_{OCS}(t)$ is then launched into an optical distribution network (ODN), which consists of a hybrid optical channel of SMF and FSO channel.

2.1 Atmospheric turbulence

Note, in SMF, the main limiting factor that deteriorates the signal quality is the CD, which results in the increased BER due to intersymbol interference (ISI). In FSO, the link performance is highly susceptible to the weather conditions, in particular by the AT, leading to fluctuations of the received irradiance I along the propagation path due to thermal variation-induced changes in the refractive index of the air. In other words, AT causes variation on both amplitude and phase of the propagating optical beam, which can result in fading and pulse distortion. The most widely used parameter as a measure of the AT strength is C_n^2 ($m^{-2/3}$), which is given by [23]:

$$C_n^2 = \left(79 \times 10^{-6}\frac{P}{T^2}\right)^2 C_T^2 \quad (4)$$

where P is the atmospheric pressure in millibar, T is the average temperature in Kelvin and C_T^2 is the temperature structure parameter, which is reliant on the temperatures at two points separated by the propagation distance d as given by [23]:

$$C_T^2 = (T_1 - T_2)^2/d^{2/3} \quad (5)$$

It is worth to mention that, C_n^2 generally varies from 10^{-17} up to 10^{-12} $m^{-2/3}$ for weak-to-strong AT regimes. Rytov variance σ_R^2 is also used to classify the AT strength, which is linearly proportional to C_n^2 as given by [23]:

$$\sigma_R^2 = 1.23 C_n^2 \left(\frac{2\pi}{\lambda}\right)^{7/6} L^{11/6} \quad (6)$$

where λ is the transmission wavelength (i.e., 1550 nm). Note that, according to Eq. (6), we could see that σ_R^2 is inversely proportional to λ. In this work, we investigate the downlink transmission in the C-band (i.e., λ ranging from 1530 to 1565 nm), where the corresponding values of σ_R^2 differ less than 3%. The wavelength dependence of AT-induced fading is therefore minor.

Weak AT is associated with $\sigma_R^2 < 1$, moderate AT with $\sigma_R^2 = 1$ and strong AT with $\sigma_R^2 > 1$. Determining σ_R^2 is critical when scaling C_n^2 in a short-range to medium- and long-distance FSO link. Fig. 3 presents the relationship of C_n^2 and σ_R^2 for different values of L. Note that, $\sigma_R^2 = 1$ and $L = 500$ m correspond to C_n^2 of about 2×10^{-13} $m^{-2/3}$, whereas extending L to 1000 and 5000 m leads to C_n^2 of 5×10^{-14} and 2.7×10^{-15} $m^{-2/3}$, respectively.

For AT-induced intensity fluctuations, two distribution models of log-normal and Gamma-Gamma (GG) for weak and weak-to-strong turbulence, respectively, are widely adopted and reported in the literature [23]. Note that, in the GG model, I is defined as the product of two statically independent random process of I_X and I_Y, which arise from the large-scale and small-scale eddies, respectively. Details of the GG model for the probability density function (PDF) of I_X and I_Y can be found in [24]. The PDF of intensity fluctuations due to AT, governed by the GG distribution is given as [23]:

$$f_{GG}(I) = \frac{2(\alpha\beta)^{\frac{(\alpha+\beta)}{2}}}{\Gamma(\alpha)\Gamma(\beta)}(I)^{\left(\frac{(\alpha+\beta)}{2}\right)-1} \times K_{\alpha-\beta}\left(2\sqrt{\alpha\beta I}\right) \quad (7)$$

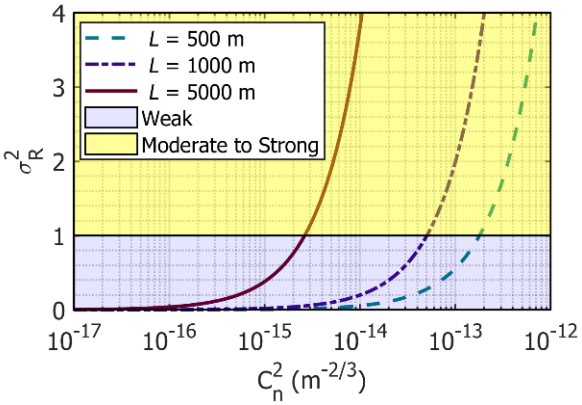

FIGURE 3. Relationship of C_n^2 and σ_R^2 for different FSO link spans.

where $\Gamma(\cdot)$ denotes the Gamma function and $K_{\alpha-\beta}(\cdot)$ is the modified Bessel function of the second kind of order $(\alpha - \beta)$. For plane wave propagation, the effective numbers representing large- and small-scale eddies of the scattering process, respectively are given by [23]:

$$\alpha = \left\{exp\left[\frac{0.49\sigma_R^2}{\left(1+1.11\sigma_R^{12/5}\right)^{5/6}}\right] - 1\right\}^{-1} \quad (8)$$

$$\beta = \left\{exp\left[\frac{0.51\sigma_R^2}{\left(1+0.69\sigma_R^{12/5}\right)^{5/6}}\right] - 1\right\}^{-1} \quad (9)$$

Fig. 4(a) presents α and β as a function of σ_R^2 for weak, moderate and strong AT regimes for L of 500 m. Note, α drops under weak AT reaching the minimum level at σ_R^2 of 1.4 and then increasing for moderate to strong AT. Whereas β is exponentially decreasing for all AT regimes. Fig. 4(b) depicts the GG PDF against I for different values of α and β and weak to strong AT regimes. Note that, plots are more skewed to the left for strong AT.

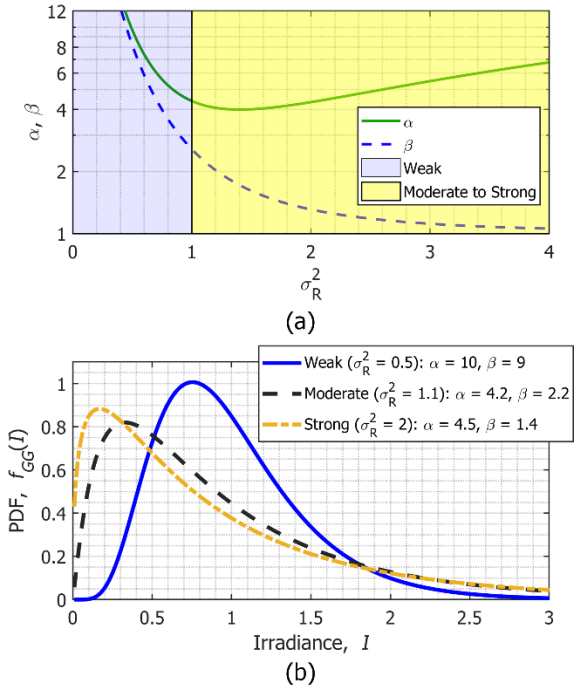

FIGURE 4. (a) Relationship of α and β and σ_R^2 and (b) Gamma-Gamma pdf for three different AT regimes.

2.2 EVM – BER performance

Following transmission over the proposed ODN, the optical signal is detected using an optical Rx composed of a high-speed PD and transimpedance amplifier for the regeneration of the mmW signal at a frequency equal to $2\omega_{LO}$, where two sidebands beating signal in (3) is held. The amplified mmW signal (using a low-noise PA) is transmitted over a free space channel by using a commercial ANT, see Fig. 2. The captured mmW signal is analyzed for the evaluation of M-QAM transmission in terms of the error vector magnitude (EVM) and the BER performance. Note, the former metric is the time-averaged root-mean-square magnitude of the error vector is given as [25]:

$$EVM_{rms}(\%) = \sqrt{\frac{\frac{1}{N}\sum_{n=1}^{N}|y[n]-x[n]|^2}{\frac{1}{N}\sum_{n=1}^{N}|x[n]|^2}} \times 100 \qquad (10)$$

where $x[n]$ is the Tx M-QAM signal, $y[n]$ is the Rx M-QAM signal and N is the total number of time samples.

For 4-, 16- and 64-QAM, the BER can be determined as, respectively [25]:

$$BER_{4-QAM} = \frac{1}{2}erfc\left(\sqrt{\frac{SNR}{2}}\right) \qquad (11)$$

$$BER_{16-QAM} = \frac{3}{8}erfc\left(\sqrt{\frac{SNR}{10}}\right) \qquad (12)$$

$$BER_{64-QAM} = \frac{7}{24}erfc\left(\sqrt{\frac{SNR}{42}}\right) \qquad (13)$$

where the SNR is given by:

$$SNR = \frac{1}{EVM^2} \qquad (14)$$

and $erfc()$ is the complementary error function.

3. EXPERIMENTAL SETUP AND RESULTS

3.1 Experimental setup

In this section, we only focus on the RoF-FSO downlink for use in BWA in rural areas. The proof-of-concept experimental setup is shown in Fig. 5, which consists of four sections of optical line terminal (OLT), CS, ODN and RBS.

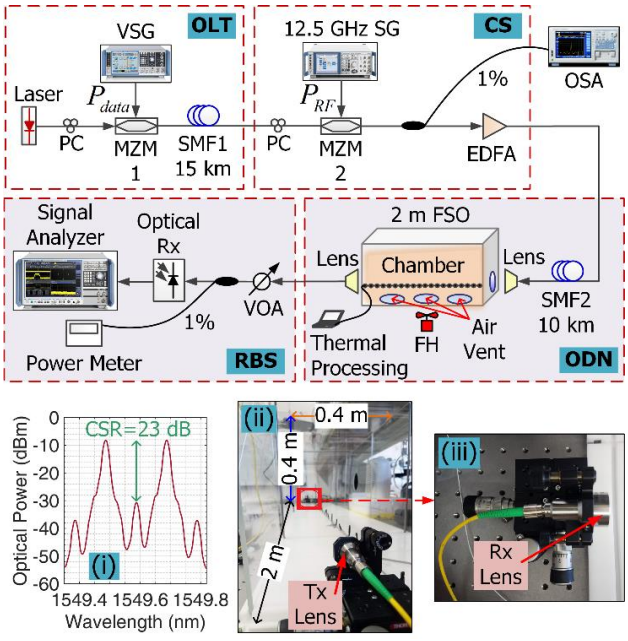

FIGURE 5. Experimental setup of a hybrid 25 GHz RoF-FSO downlink. PC: polarization controller, OSA: optical spectrum analyzer, EDFA: erbium-doped fiber amplifier, FH: fan heater and VOA: variable optical attenuator. Insets show (i) optical spectrum, (ii) turbulent chamber/Tx lens and (iii) Rx lens.

In OLT, the M-QAM signal at an intermediate frequency (IF) of 200 MHz is first generated by using a vector signal generator (R&S SMW 200A). The signal is then used for external modulation of a continuous-wave laser beam via a polarization controller (PC) and a single-drive MZM (MZM 1 – Fujitsu FTM7938EZ/201) with a half-wave voltage of 3.5 V. Note that, 4-, 16- and 64-QAM have R_b of 34, 67 and 100 Mb/s, respectively with an output power P_{data} of 7 dBm, which is chosen based on the optimization process as shown

in Fig. 6. At the power value of -4 dBm, the measured EVMs for 4-, 16- and 64-QAM are well below the corresponding required limits of 18.5, 13.5 and 9%, respectively with reference to ETSI standards [26]. It is also worth noting that, for the lower P_{data}, the EVMs between *M*-QAM signals are largely separated since the higher-order QAM formats are more sensitive to noise. The EVM is measured over 100,000 symbols and averaged over 50 EVM readings for all tests. Also depicted in insets are the resultant constellations diagrams illustrating the high-quality transmission.

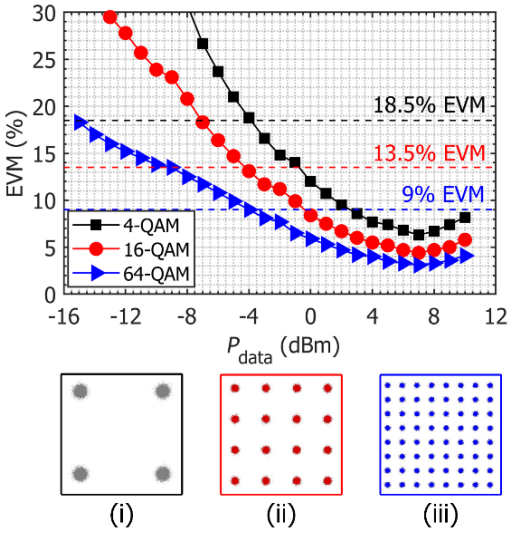

FIGURE 6. EVM versus the RF data power of *M*-QAM signals. Insets show corresponding constellation diagrams at P_{data} = 7 dBm.

The modulated signal transmitted over a SMF1 (15 km) is further externally modulated using another single-drive MZM (MZM 2 – Covega 10$^{\text{TM}}$ 081) with a half-wave voltage of 8 V by a 12.5 GHz RF clock signal from a signal generator (R&S SMF 100A) with an output power of 23 dBm. It is well-known that the physical properties of the MZM are easily affected by the change of external environment, which results in the drift of its bias point and therefore affects the performance. In this work, prior to measurements, we properly adjusted the bias voltage level applied to MZM 2 and monitored the electrical mmW spectrum over time on the signal and spectrum analyzer at the Rx. The most stable bias voltage value was adopted. Note, MZM 2 is biased at the minimum transmission point and its output optical spectrum is the two-optical-tone signal with 25 GHz frequency spacing – see inset (i) in Fig. 5. The measured CSR is 23 dB at a bias voltage of 2.9 V, which is adopted for all *M*-QAM for a fair comparison. Following amplification by an EDFA, the output of the MZM 2 is transmitted over a 10 km SMF2 to ODN. The optical signal at the SMF2 output is launched into a 2 m FSO channel via an optical lens – see insets (ii). A second lens is used at the end of the channel to capture the light for transmission over SMF – see inset (iii). Note that, both of them are air-spaced doublet lens (Thorlabs F810APC-1550) with an aperture diameter and focal length of 2.54 and 3.71 cm, respectively. The FSO link loss is about 4 dB. It is worth to mention that longer FSO distance would require advanced optical beam coupling techniques at the receiving side in order to reduce the beam size and obtain low loss coupling from a wider beam.

For the generation of non-uniform AT, an external fan heater positioned at the center of the chamber is used to blow hot air perpendicularly to the propagating light beam via a central air vent. Two air vents at each end of the chamber are used for heat dissipation (i.e., controlling the AT level). To accurately measure the thermal profiles within the chamber, 20 thermal sensors are equidistantly placed (i.e., d = 10 cm) along the chamber.

Fig. 7 shows the temperature profiles for two AT cases of low-level uniform S0 and non-uniform S1. The recorded temperature is processed offline using (4) and (5) to determine C_n^2 which is also illustrated in Fig. 7. Note, σ_R^2 can also be easily determined using (6) in order to scale the measurements for the outdoor environment. For S0, with a mean temperature of ~25˚C, the resultant C_n^2 is 5.9×10^{-14} m$^{-2/3}$. For S1, we set the highest temperatures at the center of the chamber with a peak temperature of ~47˚C and thus C_n^2 of 8.8×10^{-11} m$^{-2/3}$, which is more than three orders of magnitude higher compared to S0. Regarding the lower temperature profiles of 33 – 37˚C on either side of the chamber, the resultant C_n^2 are 6.9×10^{-12} m$^{-2/3}$ and 7.3×10^{-12} m$^{-2/3}$. At RBS, a variable optical attenuator (VOA) is used to adjust the received optical power P_r level prior to detection using a 38 GHz PIN PD (New Focus 1474-A). The regenerated mmW signal is captured using a signal and spectrum analyzer (R&S FSW) for signal assessment. All the key system parameters adopted in the experiment are presented in Table 2.

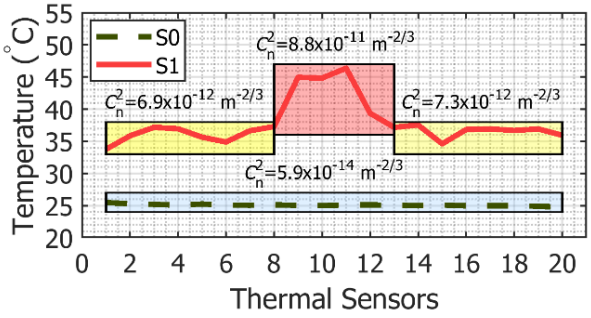

FIGURE 7. Thermal profiles in case of uniform S0 and non-uniform S1 AT.

TABLE 2. KEY PARAMETERS USED IN EXPERIMENT AND SIMULATION

Parameter	Experiment	Simulation
Laser		
• Wavelength	1549.6 nm	1550 nm
• Output power	16 dBm	16 dBm
Modulation format (R_b)	4-QAM (34 Mb/s) 16-QAM (67 Mb/s) 64-QAM (100 Mb/s)	4-QAM (10 Gb/s) 64-QAM (10 Gb/s)
mmW carrier frequency	25 GHz	25 GHz
Standard SMF		
• SMF1 length	15 km	15 km
• SMF2 length	10 km	10 km
• Dispersion	17 ps/(nm·km)	17 ps/(nm·km)
FSO		
• Aperture diameter	2.54 cm	5 cm
• Length	2 m	500 m
EDFA		
• Output power	15 dBm	6 dBm
• Noise figure	< 4 dBm	3 dBm

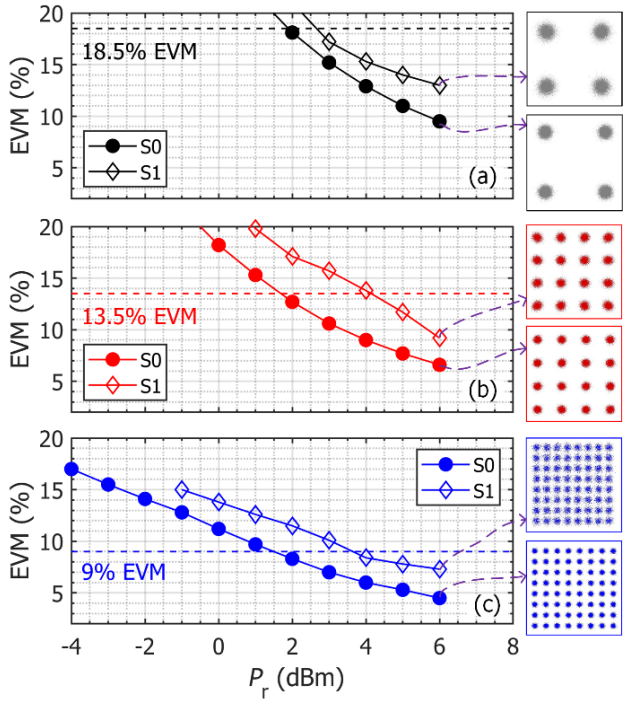

FIGURE 8. EVM versus received optical power for: (a) 4-, (b) 16- and (c) 64-QAM transmissions. Insets show corresponding constellation diagrams at P_r of 6 dBm.

3.2 Experimental results

Figs. 8(a), (b) and (c) show the measured EVMs as a function of P_r for the *M*-QAM RoF-FSO downlink under S0 and S1. For S0, the EVM values are about 9.5, 6.6 and 4.5% at P_r of 6 dBm, which increased by 3.5, 2.5 and 2.8%, respectively for S1. Note that, all EVM values are well below the corresponding required EVM limits for P_r > 4 dBm, thus confirming the practicality of the proposed RoF-FSO downlink in the PON architecture for ubiquitous coverage. In addition, we measured the *M*-QAM constellations for P_r of 6 dBm as shown in insets of Fig. 8. Note, AT results in the spreading of the symbol size, which in turn induces a power fading on the received electrical *M*-QAM spectrum. It is worth noting that in [13], we showed the power fading effect on the received 16-QAM spectrum at R_b and a mmW carrier signal of 8 Gb/s and 40 GHz, respectively by demonstrating five thermal-induced turbulent distributions along indoor FSO link.

We then further investigate the RoF-FSO downlink performance under S0 and S1 by evaluating the BER as a function of P_r for 4-, 16- and 64-QAM. The results are shown in Figs. 9(a), (b) and (c), respectively. Fig. 9 also depicts the reference line for Reed-Solomon (255, 239) FEC limit of 2×10^{-4}. As can be seen, for S0, the BER of all QAM signals is well below the FEC limit at P_r of 6 dBm. However, for S1, the BERs are more degraded, which clearly indicate the effect of non-uniform AT.

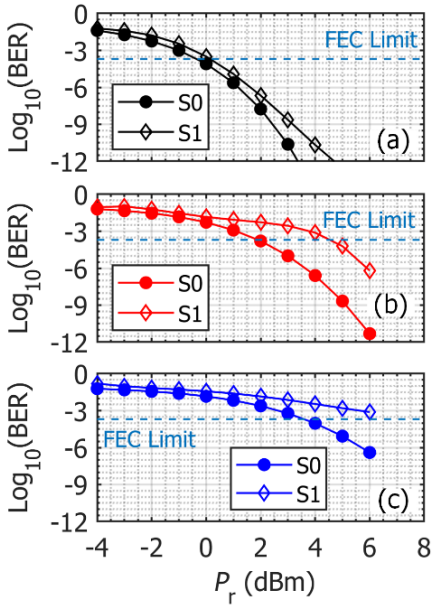

FIGURE 9. BER versus received optical power for: (a) 4-, (b) 16- and (c) 64-QAM transmissions.

Fig. 10 then shows the BER versus the received mmW power $P_{r-\mathrm{mmW}}$ for 4-, 16- and 64-QAM over the hybrid link for S0 and S1. $P_{r-\mathrm{mmW}}$ penalties between two scenarios with 4-, 16- and 64-QAM are about 1, 2 and 3 dB compared at the FEC limit, respectively. Note, power fading due to the non-uniform AT effect is also more perceptible for higher-order QAM. For S1, at the maximum $P_{r-\mathrm{mmW}}$, the corresponding BERs are $< 10^{-12}$ (error-free transmission), 4.4×10^{-7} and 8.2×10^{-4} for 4-, 16- and 64-QAM, respectively.

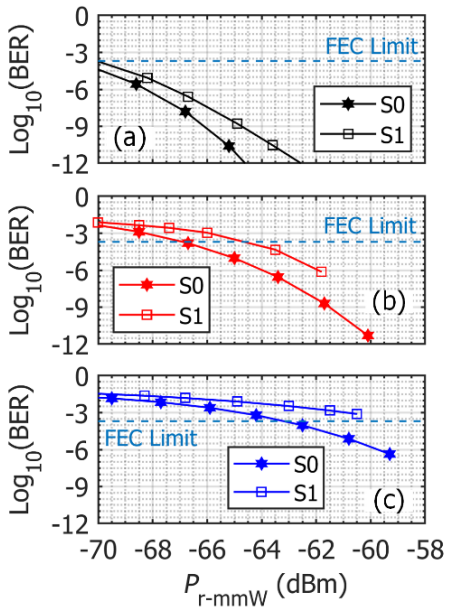

FIGURE 10. BER versus received mmW power for: (a) 4-, (b) 16- and (c) 64-QAM transmissions.

4. SIMULATION SETUP AND RESULTS

In this section, for practical implementation we perform a numerical simulation of the hybrid 25 GHz RoF-FSO downlink at R_b of 10 Gb/s, see Fig. 11, using OptiSystem and MATLAB. Note, (*i*) OLT and CS are modeled similar to the experimental setup; (*ii*) the optical power launched into a SMF2 (10 km) is 5 dBm to avoid the performance degradations due to nonlinearity-induced distortions and (*iii*) the FSO link span is extended to 500 m, which represents a typical range in the last-mile applications [6]. In addition, we simulate the case where the optical mmW signal after CS is connected to the BS(RBS) for use in BWA in urban areas. For simplicity, only 4- and 64-QAM formats are considered. Fig. 12 depicts the electrical spectra of transmitted 10 Gb/s 4- and 64-QAM at an IF of 7.5 GHz with the corresponding bandwidth values of 10 and 3.3 GHz.

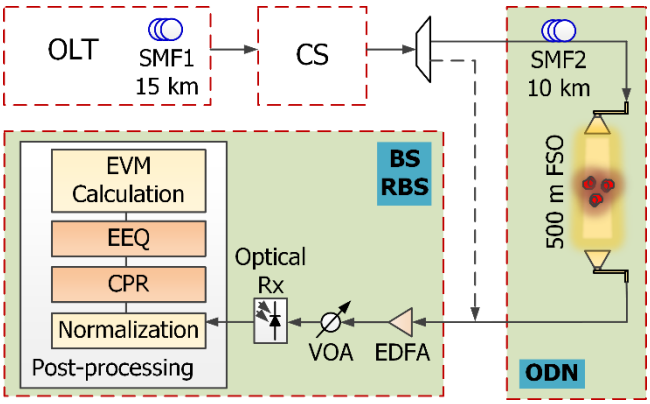

FIGURE 11. Simulation setup of a hybrid 25 GHz RoF-FSO downlink.

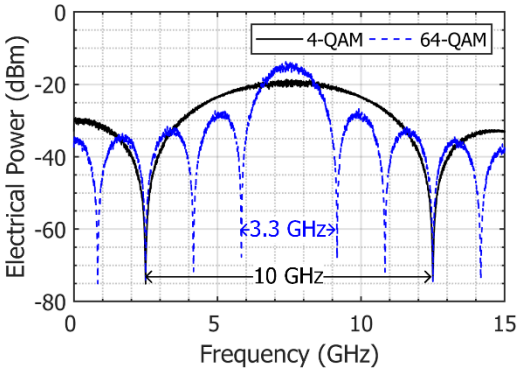

FIGURE 12. Simulated electrical spectrums of 10 Gb/s 4- and 64-QAM signals.

For the FSO channel, low-level uniform (i.e., C0) and strong non-uniform (i.e., C1) AT conditions are considered. As shown in Fig. 13, for C0, C_n^2 is 9.6×10^{-16} $m^{-2/3}$, which is a typical value for an outdoor environment. For C1, we have adopted C_n^2 values of 1.7×10^{-12} $m^{-2/3}$ and 1.6×10^{-16} $m^{-2/3}$ at the center and either end of the channel for strong and weak AT, respectively. At the BS(RBS), following amplification of the optical signal by an EDFA, the regenerated electrical signal at the optical Rx is applied to the post-processing module for normalization, optional CPR&EEQ based on the decision-directed least mean square algorithm and EVM evaluation. Note that, using traditional CPR&EEQ for mitigating the CD-induced ISI effect results in a simplified post-processing module [27].

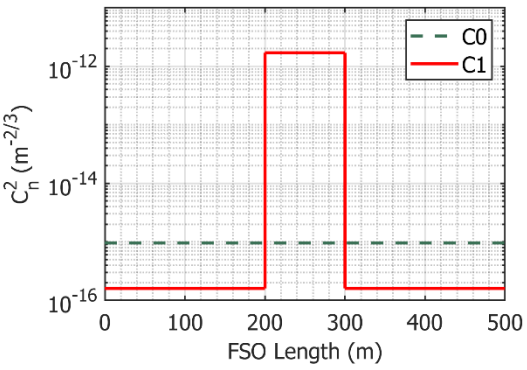

FIGURE 13. C_n^2 profiles for uniform (C0) and non-uniform (C1) AT conditions along the simulated FSO link.

4.1 Link performance evaluation for an urban area

We first present EVM results of the transmission link between OLT and BS for 10 Gb/s 4- and 64-QAM (i.e., no ODN) at P_r of 6 dBm. As can be seen in Fig. 14, the EVM values for 4- and 64-QAM are about 9.4 and 8.2%, respectively (i.e., below the EVM requirements), thus demonstrating the high-quality transmission. Note, no CPR&EEQ is applied. The constellation diagrams for 4- and 64-QAM are shown in Fig. 15(a), which are relatively clear with no rotation but to some extent, distorted, especially 64-

QAM symbols. It is worth mentioning that, the distortions are virtually more pronounced on the outer symbols, which in turn results in the pincushion distortion for 64-QAM constellation. This is because, the higher order of QAM format, the more susceptible to (*i*) noise sources (i.e., thermal and shot noise from the optical Rx) and (*ii*) ISI (i.e., CD-induced ISI in the SMF1). Even though the satisfactory EVM performance is achieved, the transmission performance however, can be significantly improved by using the optional EEQ in the post-processing module to combat the CD effect. Note, CPR is not necessary since the constellations are not rotated. Following simple linear EEQ implementation (i.e., 5-tap feed-forward equalizer (FFE)), the constellation diagrams of the received 4- and 64-QAM signals are shown in Fig. 15(b), which are well-separated with the corresponding EVM values of 5.2 and 5.5% (i.e., 4.2 and 2.7% EVM improvement compared with the case of no EEQ). Note that, a simple linear EEQ scheme can partially mitigate the distortions and therefore leaving residual ISI, especially on the outer symbols at the corners for 64-QAM constellation, which leads to the pincushion distortion slightly exists. As demonstrated in [28], ISI can be further compensated by using a maximum likelihood sequence estimation (MLSE) equalization scheme with up to 128 states or a combination of FFE and MLSE. Both techniques, however, increase the computational complexity of the post-processing module dramatically.

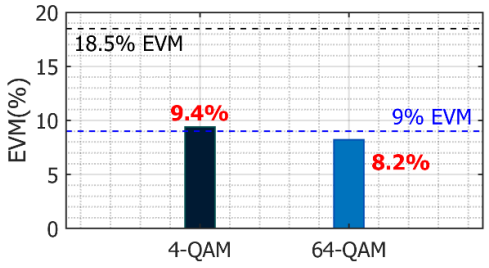

FIGURE 14. EVM values at P_r of 6 dBm for 10 Gb/s 4- and 64-QAM transmission between OLT and BS in urban areas.

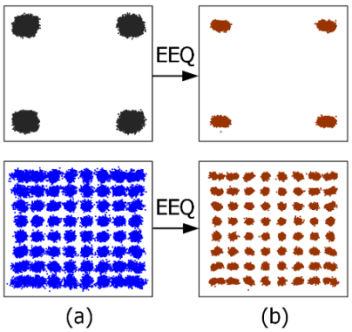

FIGURE 15. Constellation diagrams of 10 Gb/s 4- and 64-QAM: (a) without and (b) with linear EEQ.

4.2 Link performance evaluation for a rural area

In this subsection, we present results for the 10 Gb/s 4- and 64-QAM RoF-FSO downlink. Fig. 16 depicts the simulated EVM of 4-QAM together with the constellation diagrams for C0 and C1 at P_r of 6 dBm with no CPR&EEQ. Note, (*i*) for C0 the EVM is about 12.1%, which is still well below the required EVM limit of 18.5%; (*ii*) the constellation, see inset (i), is slightly rotated, which can be attributed to the different physical propagation stages at higher R_b. In fact, the optical signal was slightly distorted following transmission over the SMF1, as aforementioned; and (*iii*) the two-optical-tone signal with a frequency spacing of 25 GHz experience different propagation delay (i.e., walk-off time) following transmission over the SMF2 (i.e., 10 km), thus leading to the received signals experiencing further ISI. The observed constellation rotation effect caused by CD is in good agreement with the experimental data for both high-speed optical fiber and RoF transmission links using *M*-QAM reported in [27], [29].

For C1, the EVM penalty is 2.1% compared with C0, as shown in Fig. 16. Since EVM values of 4-QAM for C0 and C1 are below the EVM limit of 18.5%, which eases post-processing implementation, then there is no need for employing CPR&EEQ. Also shown in inset (ii), is the constellation diagram for C1, which is spread-out compared to a typical constellation. This corresponds to experimental results as presented in Section III, in which the effect of non-uniform AT is more severe compared with uniform AT. In addition, the constellation, however shows no further rotation, thus matching well with the recent experimental data on high-speed 4-QAM transmission over 100 m FSO under strong AT ($C_n^2 = 3 \times 10^{-12}$ m$^{-2/3}$) [30]. Note that, the EVM penalties for the proposed link with ODN for ubiquitous coverage in rural areas with C0 and C1 are 2.7 and 4.8%, respectively compared with urban areas, see Fig. 14.

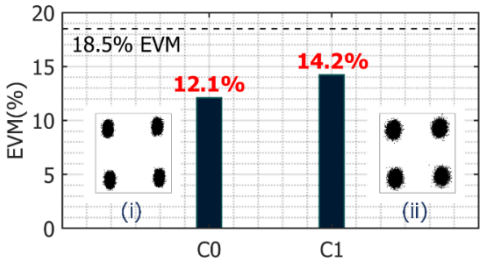

FIGURE 16. EVM obtained at P_r of 6 dBm after 10 Gb/s 4-QAM transmission to RBS in rural areas. Insets (i) and (ii) show corresponding constellation diagrams under C0 and C1. CPR&EEQ are not employed in this case.

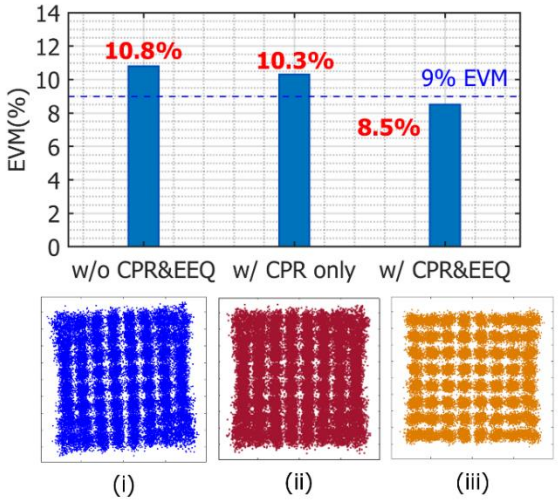

FIGURE 17. EVM obtained at P_r of 6 dBm under C1 without and with CPR only and with CPR&EEQ after 10 Gb/s 64-QAM transmission to RBS in rural areas. Insets show corresponding constellation diagrams.

Next, we evaluated the EVM performance of 10 Gb/s 64-QAM for C1 only at P_r of 6 dBm. As can be seen in Fig. 17, with no CPR&EEQ, the EVM is 10.8%, which is higher than the required 9%. This can be further perceived via the constellation diagram shown in the inset (i), which is both marginally rotated and distorted as higher-order QAM signals are more vulnerable to channel impairments. For performance improvement, we first applied CPR only to correct the phase rotation, see inset (ii), and noticed EVM enhancement by 0.5%. Linear EEQ (i.e., 5-tap FFE) is consequently applied to separately alleviate the residual CD-induced ISI in SMF2 (i.e., 10 km), which in turn leads to an EVM of 8.5% (i.e., below the EVM requirement). Therefore, the constellation diagram shown in inset (iii) is less distorted. Since AT is non-deterministic event, a simple linear EEQ is then not a viable option to mitigate AT-induced distortions. However, this detrimental effect can be compensated by using multiple-input-multiple-output EEQ as in [30], but at the cost of high computational complexity of the post-processing module.

In the following, we investigate the attainable mmW transmission distance between two ANTs, see Fig. 2, based on $P_{r-\mathrm{mmW}}$, which is about -20 dBm for this case (i.e., EVM of 8.5%). Using the VOA to adjust P_r and therefore $P_{r-\mathrm{mmW}}$ as shown in Figs. 8 and 9, we have estimated $P_{r-\mathrm{mmW}}$ to be about -23 dBm at the EVM of 9%, which is comparable to the experimental results reported in [31]. The maximum attainable transmission distance therefore, can be simply estimated by setting the Rx's sensitivity to $P_{r-\mathrm{mmW}}$, following mmW propagation at an EVM of 9%. Considering the predicted propagation loss according to Friis transmission, clear weather, commercial K-band Tx PA and conical horn ANTs detailed in Table 3, Fig. 18 shows the received mmW power as a function of the transmission distance for a range of transmit powers P_t. For P_t of 2 dBm (i.e., no PA), the maximum wireless transmission range is about 4 m, which is significantly increased for higher values of P_t. For P_t of 32 dBm (i.e., employing a well-developed K-band PA with a gain of 30 dB), the link span is increased by 131 m, which is sufficiently long for indoor and last-mile applications in rural areas.

TABLE 3. LINK BUDGET AND DISTANCE FOR 25 GHZ MMW TRANSMISSION

Parameter	Value
Modulation format (R_b)	64-QAM (10 Gb/s)
Atmospheric attenuation (dB/km)	0.016
EVM	9%
Rx sensitivity (dBm)	-23
Tx PA gain	0, 10, 20, 30
Tx and Rx antenna gains (dBi)	25
P_t (dBm)	2, 12, 22, 32
Max. transmission range (m)	5, 14, 43, 135

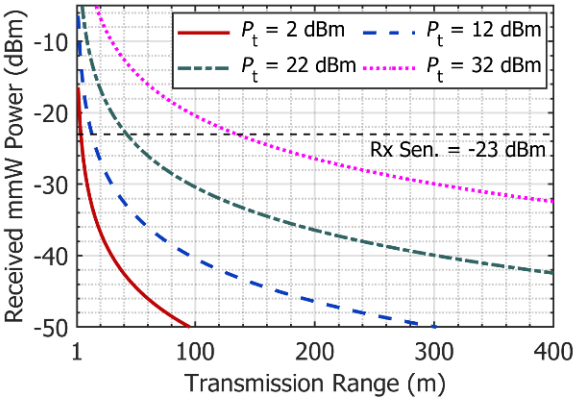

FIGURE 18. Achievable wireless transmission distance with different transmit powers for 10 Gb/s 64-QAM signal. Horizontal dash line is the benchmark Rx sensitivity of -23 dBm estimated at an EVM of 9%.

5. CONCLUSION

In this paper, for the first time we investigated a hybrid 25 GHz RoF and RoFSO downlink in a PON architecture using the MZM-based optical up-conversion technique and 4/16/64-QAM for ubiquitous BWA connectivity in urban and rural areas. We also investigated the FSO link under non-uniform turbulence for *M*-QAM and showed EVMs of 13, 9.2 and 7.3% at BER values of $< 10^{-12}$, 4.4×10^{-7} and 8.2×10^{-4} for *M* of 4, 16 and 64, respectively with clear constellation diagrams, thus demonstrating the use of the proposed scheme for practical applications. For practical outdoor environments, we carried out a number of simulations for 10 Gb/s 4- and 64-QAM over an extended FSO link span of 500 m under non-uniform turbulence. We showed that, there is a good agreement between experimental and simulation results. By using simple carrier phase recovery and linear electrical equalization schemes to separately compensate for the CD, we achieved EVM values of 14.2 and 8.5% for 4- and 64-QAM, which are well below the EVM limits of 18.5 and 9%, respectively according to the ETSI standards. A maximum wireless transmission distance of

about 135 m was achieved by employing a commercial K-band PA and a pair of horn ANTs with the gain of 30 dB and 25 dBi each, respectively.

Declaration of competing interest

The authors declare that they have no known competing financial interests or personal relationships that could have appeared to influence the work reported in this paper.

Acknowledgements

This work was supported in part by the Ministry of Education, Youth and Sports of Czech Republic (CZ.02.2.69/0.0/0.0/16_027/0008465), and in part by European Cooperation in Science and Technology COST CA16220 and CTU project SGS20/166/OHK3/3T/13.

References

[1] X. Li, J. Yu, Z. Zhang, J. Xiao, and G. K. Chang, "Photonic vector signal generation at W-band employing an optical frequency octupling scheme enabled by a single MZM," *Opt. Commun.*, vol. 349, pp. 6–10, 2015.

[2] T. Kawanishi, "THz and photonic seamless communications," *J. Lightwave Technol.*, vol. 37, no. 7, pp. 1671–1679, 2019.

[3] X. Li, J. Yu, and G.-K. Chang, "Photonics-aided millimeter-wave technologies for extreme mobile broadband communications in 5G," *J. Lightwave Technol.*, vol. 38, no. 2, pp. 366–378, Jan. 2020.

[4] H. Y. Wang, C. H. Cheng, C. T. Tsai, Y. C. Chi, and G. R. Lin, "28-GHz wireless carrier heterodyned from orthogonally polarized tri-color laser diode for fading-free long-reach MMWoF," *J. Lightwave Technol.*, vol. 37, no. 13, pp. 3388–3400, 2019.

[5] M. A. Khalighi and M. Uysal, "Survey on free space optical communication: a communication theory perspective," *IEEE Commun. Surv. Tutorials*, vol. 16, no. 4, pp. 2231–2258, 2014.

[6] "KORUZA Transceivers." [Online]. Available: http://www.koruza.net/.

[7] H. H. Refai, J. J. Sluss, Jr., and H. H. Refai, "Comparative study of the performance of analog fiber optic links versus free-space optical links," *Opt. Eng.*, vol. 45, no. 2, p. 025003, Feb. 2006.

[8] P. T. Dat *et al.*, "Studies on characterizing the transmission of RF signals over a turbulent FSO link," *Opt. Express*, vol. 17, no. 10, p. 7731, 2009.

[9] Y. Alfadhli *et al.*, "Real-time FPGA demonstration of hybrid bi-directional MMW and FSO fronthaul architecture," in *2019 Optical Fiber Communications Conference and Exhibition, OFC 2019 - Proceedings*, 2019, p. W2A.39.

[10] P. T. Dat, A. Kanno, K. Inagaki, T. Umezawa, N. Yamamoto, and T. Kawanishi, "Hybrid optical wireless-mmWave: ultra high-speed indoor communications for beyond 5G," in *IEEE INFOCOM 2019 - IEEE Conference on Computer Communications Workshops (INFOCOM WKSHPS)*, 2019, pp. 1003–1004.

[11] M. A. Esmail, A. Ragheb, H. Fathallah, and M.-S. Alouini, "Investigation and demonstration of high speed full-optical hybrid FSO/fiber communication system under light sand storm condition," *IEEE Photonics J.*, vol. 9, no. 1, pp. 1–12, Feb. 2017.

[12] D.-N. Nguyen, J. Bohata, M. Komanec, S. Zvanovec, B. Ortega, and Z. Ghassemlooy, "Seamless 25 GHz transmission of LTE 4/16/64-QAM signals over hybrid SMF/FSO and wireless link," *J. Lightwave Technol.*, vol. 37, no. 24, pp. 6040–6047, 2019.

[13] L. Vallejo *et al.*, "Impact of thermal-induced turbulent distribution along FSO link on transmission of photonically generated mmW signals in the frequency range 26–40 GHz," *IEEE Photonics J.*, vol. 12, no. 1, pp. 1–9, Feb. 2020.

[14] I. A. Alimi, A. L. Teixeira, and P. P. Monteiro, "Toward an efficient C-RAN optical fronthaul for the future networks: A tutorial on technologies, requirements, challenges, and solutions," *IEEE Commun. Surv. Tutorials*, vol. 20, no. 1, pp. 708–769, 2018.

[15] N. Iiyama, S.-Y. Kim, T. Shimada, S. Kimura, and N. Yoshimoto, "Co-existent downstream scheme between OOK and QAM signals in an optical access network using software-defined technology," in *OFC/NFOEC 2012 - Optical Fiber Communication and the National Fiber Optic Engineers Conference*, 2012, vol. 1, p. JTh2A.53.

[16] C. H. Yeh, W. P. Lin, C. M. Luo, Y. R. Xie, Y. J. Chang, and C. W. Chow, "Utilizing single lightwave for delivering baseband/fso/mmw traffics simultaneously in pon architecture," *IEEE Access*, vol. 7, pp. 138927–138931, 2019.

[17] D. T. Van Veen, V. E. Houtsma, A. H. Gnauck, and P. Iannone, "Demonstration of 40-Gb/s TDM-PON over 42-km with 31 dB optical power budget using an APD-based receiver," *J. Lightwave Technol.*, vol. 33, no. 8, pp. 1675–1680, 2015.

[18] S. Rodríguez, S. Rommel, J. J. Vegas Olmos, and I. T. Monroy, "Reconfigurable radio access unit to dynamically distribute W-band signals in 5G wireless access networks," *Opt. Switch. Netw.*, vol. 24, no. October 2016, pp. 21–24, 2017.

[19] R. Chuenchom *et al.*, "Hybrid fiber wireless (HFW) extension for GPON toward 5G," in *Optical and Wireless Convergence for 5G Networks*, Wiley, 2019, pp. 31–55.

[20] J. R. Barry, *Wireless infrared communications*. Boston, MA: Springer US, 1994.

[21] J. Yu, Z. Jia, L. Yi, Y. Su, G.-K. Chang, and T. Wang, "Optical millimeter-wave generation or up-conversion using external modulators," *IEEE Photonics Technol. Lett.*, vol. 18, no. 1, pp. 265–267, 2006.

[22] J. Ma, J. Yu, C. Yu, X. Xin, J. Zeng, and L. Chen, "Fiber dispersion influence on transmission of the optical millimeter-waves generated using LN-MZM intensity modulation," *J. Lightwave Technol.*, vol. 25, no. 11, pp. 3244–3256, 2007.

[23] L. C. Andrews and R. L. Phillips, *Laser beam propagation through random media*, vol. 1. 1000 20th Street, Bellingham, WA 98227-0010 USA: SPIE, 2005.

[24] Z. Ghassemlooy, W. O. Popoola, and S. Rajbhandari, *Optical wireless communications – system and channel modelling with*

Matlab, 2nd ed. Cham: CRC Press, 2019.

[25] C. H. Lee, *Microwave photonics*, 2nd ed. CRC Press, 2013.

[26] "Universal Mobile Telecommunications System (UMTS); LTE; Active Antenna System (AAS) Base Station (BS) conformance testing; Part 1: conducted conformance testing (3GPP TS 37.145-1 version 14.1.0 Release 14)," 2017.

[27] Y. Wang, J. Yu, X. Li, Y. Xu, N. Chi, and G.-K. Chang, "Photonic vector signal generation employing a single-drive MZM-based optical carrier suppression without precoding," *J. Lightwave Technol.*, vol. 33, no. 24, pp. 5235–5241, 2015.

[28] F. Karinou, N. Stojanovic, A. Daly, C. Neumeyr, and M. Ortsiefer, "1.55-µm long-wavelength VCSEL-based optical interconnects for short-reach networks," *J. Lightwave Technol.*, vol. 34, no. 12, pp. 2897–2904, 2016.

[29] S. Almonacil, P. Jenneve, P. Ramantanis, and P. Layec, "A novel constellation phase rotation method to reduce transmitter noise in metro links," *IEEE Photonics Technol. Lett.*, vol. 30, no. 16, pp. 1459–1462, 2018.

[30] L. Li *et al.*, "Mitigation for turbulence effects in a 40-Gbit/s orbital-angular-momentum-multiplexed free-space optical link between a ground station and a retro-reflecting UAV using MIMO equalization," *Opt. Lett.*, vol. 44, no. 21, p. 5181, Nov. 2019.

[31] A. Kanno *et al.*, "Coherent radio-over-fiber and millimeter-wave radio seamless transmission system for resilient access networks," *IEEE Photonics J.*, vol. 4, no. 6, pp. 2196–2204, 2012.